Non-peer-reviewed EarthArXiv preprint; submitted to Remote Sensing of Environment (Elsevier).

Land subsidence in Jakarta in Three Dimensions (2014–2025) using InSAR–GNSS Datum Connection and the Strapdown Decomposition

Alexandru M. Lapadat[a,*], Heri Andreas[b], Wietske S. Brouwer[a], Simon A.N. van Diepen[a], Dhota Pradipta[b], Ramon F. Hanssen[a]

[a] *Mathematical Geodesy and Positioning, Delft University of Technology, Stevinweg 1, Delft, Netherlands*
[b] *Geodesy Research Division, Institute of Technology Bandung, Jl. Ganesha 10, Bandung, Indonesia*

Abstract

Coastal megacities face compounding hazards from rising sea levels and land subsidence. Jakarta, one of the fastest-sinking megacities, already experiences recurrent flooding amplified by rapid land subsidence. Assessing and mitigating this hazard requires reliable estimates of three-dimensional ground motion over wide spatial and temporal scales in a well-defined geodetic reference frame and datum. Here we combine spaceborne InSAR and GNSS measurements. We develop a datum connection procedure that aligns multi-track InSAR line-of-sight datasets between 2014 and 2025 to a common datum for unbiased three-dimensional velocity decomposition, and connect the resulting displacement field to the Sunda plate-fixed frame using GNSS, yielding a 3D characterization of Jakarta's land deformation in a globally consistent reference frame. Our results show that Jakarta's land motion is dominated by six main subsidence bowls, with subsidence and directional horizontal rates of up to −7.9 cm/yr and 1.7 cm/yr, respectively, overlying slow regional subsidence of −0.9 cm/yr across the metropolitan area. As these results hinge

*Corresponding author
Email address: A.M.Lapadat@tudelft.nl (Alexandru M. Lapadat)

on the availability of one single continuous GNSS station, we recommend the installation of dedicated geodetic ground-based infrastructure to ensure sustainable and rigorous monitoring capabilities for the future.

Keywords: InSAR, GNSS, datum, geodesy, land subsidence, Jakarta

1. Introduction

Jakarta, the world's most populous city with close to 42 million residents (United Nations, 2025), is among the fastest-sinking megacities on Earth. Historically, using observations since 1925 (Schepers, 1926; Schuitenvoerder, 1926), subsidence occurred at two distinct scales: a citywide north-dipping tilt spanning ∼30 km[1], with rates declining from −4.5 cm/yr in the north to near-zero in the south, and localized subsidence bowls superimposed on this trend, whose extent and intensity vary spatiotemporally, with maximum rates ranging from −7 to −15 cm/yr (Abidin et al., 2001, 2011, 2022). Currently, ∼15% of Jakarta's land area—mainly in the northern districts—already lies below mean sea level, leaving these areas prone to inundation during ordinary high tides (Juliandri et al., 2022). While citywide catastrophic floods in the past decade have been mostly driven by extreme rainfall and river runoff, in North Jakarta it is the subsidence that is causing recurrent tidal flooding, a risk further intensified by ongoing regional sea-level rise (Fenoglio-Marc et al., 2012). Jakarta's subsidence is attributed to three interacting mechanisms: (i) natural compaction of young Quaternary coastal alluvium, (ii) increased effective stress from the load of dense urban development and infrastructure, and (iii) groundwater extraction, which reduces pore pressure in the aquifer system and induces localized, bowl-shaped subsidence (Murdohardono and Sudarsono, 1998; Abidin et al., 2001; Colbran, 2009; Batubara et al., 2023). While natural compaction and loading act gradually, groundwater withdrawal produces rapid and spatially concentrated deformation. The combined effects are structural damage to buildings, cracking and tilting (Abidin et al., 2015; Nugraha et al., 2024), and recurrent flooding (Takagi et al., 2016; Sagala et al., 2013; Firman et al., 2011; Lubis et al., 2022), making land subsidence one of the most critical hazards for Jakarta's long-term sustainability. The combined processes (Abidin et al., 2022; Bennett et al., 2023; Lubis et al., 2022; Colbran, 2009; Takagi et al., 2016; Sagala et al., 2013; Firman et al.,

[1]from Ancol to Pasar Rebo

2011) of land subsidence, sea-level rise, extreme precipitation, and runoff put Jakarta at risk, with subsidence amplifying hazards by lowering ground elevation, increasing coastal flood exposure, and accelerating runoff. These impacts make precise estimation and continuous monitoring of land subsidence essential for effective risk assessment and flood mitigation (Abidin et al., 2015).

Over the past four decades, a range of geodetic techniques (Abidin et al., 2004) have been applied, each with distinct strengths and limitations. Spirit leveling in the 1980s (Abidin et al., 2001; Ekkelenkamp, 2019; Schepers, 1926; Schuitenvoerder, 1926) provided millimeter-level precision but was costly, slow, and spatially sparse. Of the 45 benchmarks established in 1982 (Abidin et al., 2001), many have since disappeared due to Jakarta's rapid urban development. GNSS campaigns from the 1990s onward (Abidin et al., 2001, 2008; Abdullah et al., 2021; Susilo et al., 2023) expanded from 13 benchmarks to 65 by 2010, improving spatial coverage and revealing broader subsidence patterns, but in the meantime several benchmarks became unobservable due to monument destruction (Abidin et al., 2011). Thus, for both leveling and GNSS, the loss or inaccessibility of benchmarks limits the temporal continuity and spatial completeness of the subsidence record. The introduction of spaceborne Interferometric Synthetic Aperture Radar (InSAR) (Hanssen, 2001) in the 1990s revolutionized monitoring, offering dense spatial coverage and frequent temporal sampling across Jakarta's metropolitan area (Abidin et al., 2005, 2011). Early InSAR studies (Abidin et al., 2005; Ng et al., 2012; Koudogbo et al., 2012; Chaussard et al., 2013; Widodo et al., 2019) from Jakarta relied on short, single-track SAR datasets and suffered from temporal decorrelation (Zebker and Villasenor, 1992). Advances in processing methods (e.g., Persistent Scatterer Interferometry (PSI) (Ferretti et al., 2002b,a) and Small Baseline Subset (SBAS) (Berardino et al., 2003; Hooper, 2008)) combined with greater computational capacity, have enabled longer time series and multi-track coverage (Hakim et al., 2020; Zhang et al., 2025; Sidiq et al., 2025).

As InSAR observes the projection of the 3D displacement vector onto the radar line of sight (LoS), often these estimates were projected onto the vertical (PoV), an error-free operation only if horizontal displacements are negligible (Brouwer and Hanssen, 2023). Consequently, vertical PoV displacements are biased in localized subsidence bowls. Harintaka et al. (2024) combined ascending and descending tracks to estimate the projection of the displacement onto the East–Up plane, still biased (Brouwer and Hanssen,

2023). Therefore, no InSAR product currently provides a complete three-dimensional and unbiased view of ground motion in Jakarta.

Nearly all InSAR-based velocity maps of Jakarta are relative, given in an arbitrary local InSAR datum. The physical 'null-location', where the displacement rate is 0 mm/yr, is unknown. This rank defect can result in misleading geophysical interpretations, such as apparent uplift in central Jakarta (Widodo et al., 2019; Zhang et al., 2025), which is physically unrealistic. Consequently, studies focusing on fast-subsiding bowls driven by groundwater extraction may overlook slower, widespread regional subsidence, which can be obscured if the InSAR datum is not linked to a plate-fixed reference frame, such as the Sunda plate-fixed frame (Yong et al., 2017). In fact, only a few studies have rigorously explored geodetic datum connections that link InSAR to a terrestrial reference frame using GNSS (Mahapatra et al., 2018; Su et al., 2026), underscoring the need for a robust 3D datum connection procedure.

Using a modified strapdown decomposition (Brouwer and Hanssen, 2024)—aligning multi-track InSAR data to a common datum and connecting InSAR-derived land motion with GNSS to a global reference frame—we present the first estimation of three-dimensional velocity vectors across Jakarta in the Sunda plate-fixed frame. In Sec. 2 we present the input datasets and the methodology for multi-track InSAR alignment and the datum connection of the InSAR velocity map to the Sunda plate-fixed frame using GNSS. In Sec. 3, we apply the method to two InSAR track velocity datasets to obtain 3D velocities aligned to a common InSAR datum. We then estimate the velocity offset between this local InSAR datum and the Sunda plate-fixed frame at the location of a continuously operating GNSS reference station (CORS) and apply it uniformly to all provisory 3D velocities, producing the final 3D velocity field for Jakarta in the Sunda plate-fixed frame. Sec. 4 presents the resulting subsidence patterns, and the final section summarizes the key findings and their implications for Jakarta.

2. Methodology

We subsequently discuss the input datasets and the decomposition assumptions, followed by the inter-track datum alignment establishing a common InSAR datum, and a methodology for estimating the motion of this common InSAR datum within the Sunda plate-fixed frame.

2.1. Dataset Preparation

We use two datasets of linear velocities estimated from InSAR Point Scatterer[2] (PS) LoS displacement time series spanning 2014–2025, see Fig. 1. The datasets were generated from 281 Sentinel-1 acquisitions from ascending

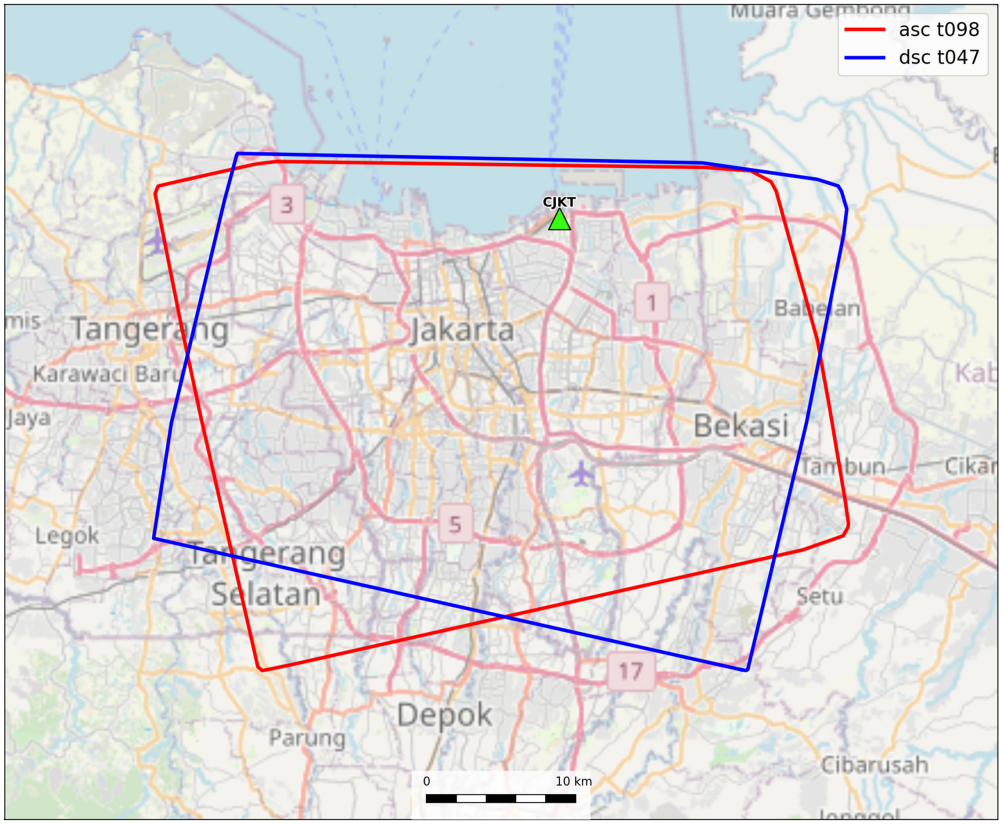

Figure 1: Area of Interest (AOI) covering the Jakarta metropolitan area, showing the Sentinel-1 ascending (track 98, red) and descending (track 47, blue) footprints. The location of the CORS GNSS station CJKT used for datum alignment is indicated as a green triangle.

track 98 and 183 acquisitions from descending track 47, using the Delft implementation of Persistent Scatterer Interferometry, DePSI (Kampes, 2006; Van Leijen, 2014). Visual inspection and post-fit residual analysis of the LoS displacement time series show that the deformation is predominately

[2]We use the Delft taxonomy for scatterer classification, see (Hu et al., 2019)

linear over 2014–2025. A linear velocity model is therefore adopted for all subsequent estimates. Each track uses a unique local datum defined by its mean linear velocity. Consequently, all velocities are relative and must be interpreted in terms of the spatial variability.

Additionally, we use GNSS data from station CJKT, see Figs. 1 and 2, a long-term CORS to align the common InSAR datum with the Sunda plate-fixed frame. CJKT is located at Tanjung Priok and operated by Badan Informasi Geospasial (BIG), with its antenna mounted on a 2 m tall cast-concrete pillar on the roof of a two-story concrete building, see Fig. 2D. It is the only existing CORS station in Jakarta that was operational during the 2014–2025 period. The daily station coordinates were derived from continuous GPS phase observations collected between October 2010 and January 2022. The GNSS data were processed by Susilo et al. (2023) in differential mode using the GAMIT/GLOBK software package version 10.71 (Herring et al., 2010). Daily station positions were estimated using double-differenced, ionosphere-free phase observations with respect to 12 IGS reference stations. This yields station coordinates in ITRF2014, applying precise IGS orbits, atmospheric delay modeling, and standard tidal and loading corrections. The daily solutions were subsequently combined and aligned in GLOBK to the IGb14[3] using eight stable global reference stations.

To express the GNSS time series in the Sunda plate-fixed frame, we removed the rigid motion of the Sunda Plate from the IGb14 coordinates using the GSRM v2.1 plate-motion model (Kreemer et al., 2014)[4]. The horizontal velocity of the Sunda Plate at CJKT was computed at epoch 2016.66, linearly propagated over the IGb14 displacements time span, and subtracted from the displacement time series, see Fig. 2A–C.

The 3D displacement time series of CJKT, together with their 2σ uncertainties were subsampled over 2014–2022 to match the InSAR observation period and used to estimate linear 3D velocities in the Sunda plate-fixed frame, assuming a constant displacement rate consistent with the InSAR analysis. These 3D velocities are used to tie the relative InSAR velocity estimate to the Sunda plate-fixed frame for land-subsidence analysis. The resulting velocities in both reference frames are summarized in Tab. 1

[3]International GNSS Service (IGS) reference frame aligned with ITRF2014.

[4]Euler pole and angular velocity, IGS08 realization.

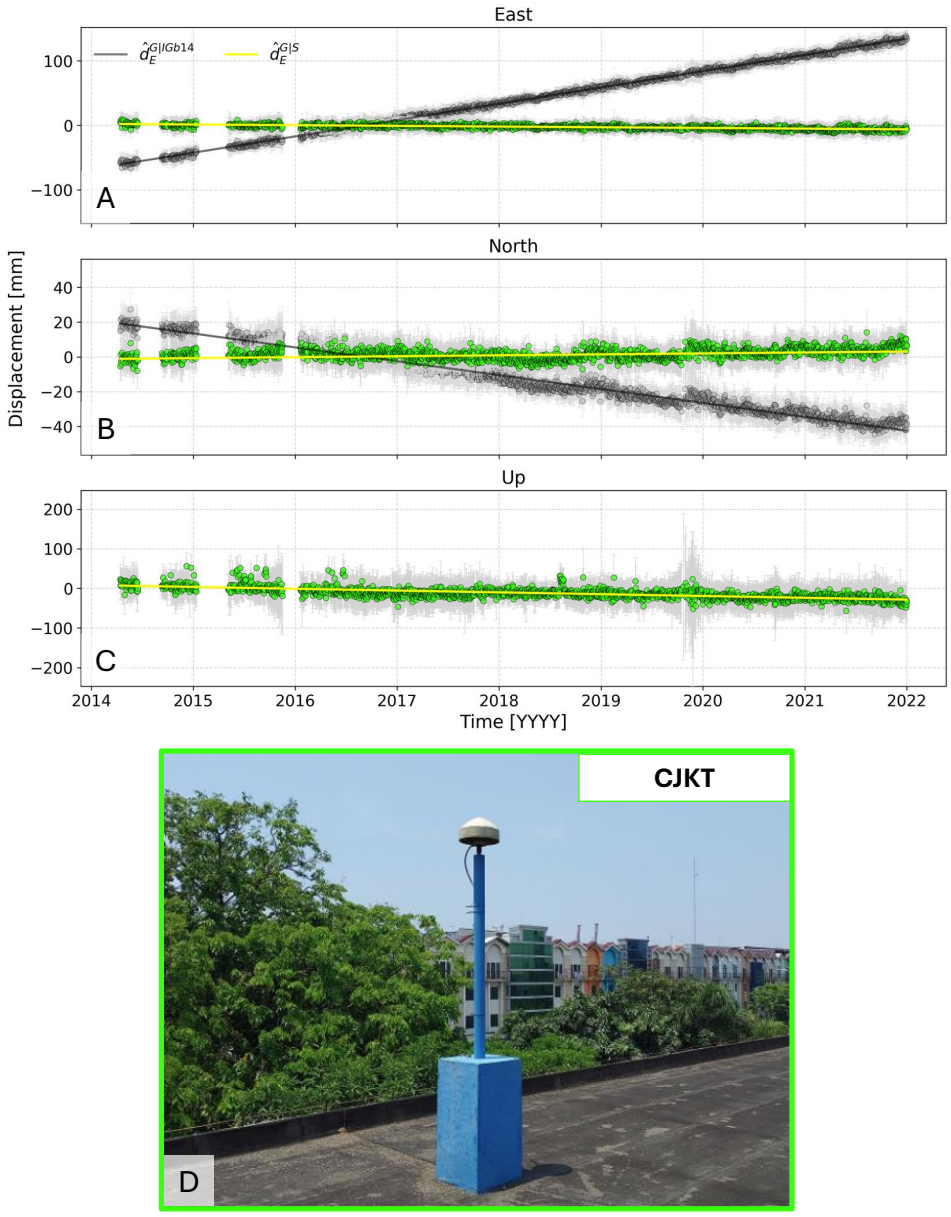

Figure 2: (A–C) East, North, and Up displacement time series of the CJKT GNSS station (2014–2022) with 2σ uncertainties. Grey markers show IGb14 displacements, while green markers show the time series expressed in the Sunda plate-fixed frame after removing Sunda Plate motion using the GSRM v2.1 model. This removal eliminates the southeast horizontal plate motion of 26.52 ± 0.05 mm/yr, yielding near-zero horizontal velocity. The corresponding 3D linear velocities in both reference frames are reported in Tab. 1. (D) Photograph of the CJKT GNSS installation and pillar, located on the roof of a two-story concrete building with a likely deep foundation.

Component	$\hat{d}^{G\|\mathrm{IGb14}}$ [mm/yr]	$\hat{d}^{G\|\mathrm{S}}$ [mm/yr]
East	25.28 ± 0.05	-1.06 ± 0.05
North	7.99 ± 0.04	0.54 ± 0.04
Up	-4.6 ± 0.2	-4.6 ± 0.2

Table 1: Linear velocities of the CJKT GNSS station in the IGb14 ($\hat{d}^{G|\mathrm{IGb14}}$) and Sunda Plate-fixed ($\hat{d}^{G|\mathrm{S}}$) reference frames, corresponding to the linear models fitted to the displacement time series in Fig. 2, with 2σ uncertainties. The Sunda plate-fixed frame values show small residual horizontal motion after plate-motion removal, likely reflecting limitations of the plate-motion model or local monument motion.

2.2. LoS decomposition to 3D velocity

To convert the InSAR LoS velocities (see Sup. los_velocity_input.png), into physically meaningful 3D components, we apply the strapdown decomposition method (Brouwer and Hanssen, 2024, 2021), which transforms ascending and descending LoS observations into a local transversal-longitudinal-normal (TLN) coordinate system (Chang et al., 2018), and subsequently to an East-North-Up (ENU) coordinate system (Brouwer and Hanssen, 2024).

The method assumes that deformation within each region of uniform motion (RUM), defined here as a 450×450 m area, is spatially constant, i.e., all PS within the RUM share the same displacement behavior and average linear velocity. The RUM size of 450×450 m is chosen as a trade-off between preserving homogeneous spatial deformation within each RUM and providing sufficient spatial sampling for reliable statistics, ensuring a minimum of 50 PS per track per RUM while limiting the averaging of local velocity variability. For the strapdown decomposition, the input observations consist of track-specific RUM-averaged velocities, see Sup. A, computed as the robust median[5] of all PS LoS velocities within each RUM. This yields two representative velocities per RUM, one per viewing geometry, which serve as the observations for the decomposition. Ideally, the velocity variability and contributing PS within each RUM should be evaluated on their own merit, discarding anomalous PS where justified, as will be done for the RUM used to connect to the Sunda plate-fixed frame Ṡecond, as the local TLN-frame is right-handed with the longitudinal direction tangential to

[5]The median is inherently robust, meaning it is unaffected by point scatterers that deviate strongly from the RUM median velocity (beyond ±2 times the median absolute deviation (MAD)).

the iso-displacement contours and the transversal direction defined positive down-slope, i.e., in the direction of increasing subsidence, it postulates that all transversal estimates are positive.

The initial TLN coordinate system orientation (Brouwer and Hanssen, 2024) is approximated using three angles: Λ, the azimuth of the longitudinal direction relative to geographic north, initialized by computing the 2D gradient of LoS velocities projected onto the vertical; Φ, the elevation angle of the longitudinal direction relative to the horizontal; and Ω, the elevation angle of the transversal direction. Based on Jakarta's relatively flat terrain, with topographic slopes less than 2° (Abidin et al., 2005), we assume and set $\Phi = \Omega = 0$. Conservative uncertainties of $\sigma_\Lambda = 10°$, and $\sigma_\Phi = \sigma_\Omega = 3°$ are assigned to account for potential imperfections in the TLN orientation, yielding quality metrics for the ENU displacement velocity estimates.

A concise mathematical description of the strapdown decomposition, including the observation equations and uncertainty propagation is given in Sup. A.

2.3. Inter-track InSAR datum alignment

The strapdown method requires the contributing InSAR viewing geometries to be expressed in a common datum. In the absence of terrestrial control points for inter-track datum connection, we exploit a physical constraint characteristic of subsiding regions: *transversal velocities must be centripetal, i.e., directed toward increasing subsidence* (Kratzsch, 2012). A mismatch between track datums alters both the magnitude and sign of the decomposed velocities (transversal, $\hat{d}_T$, and normal, $\hat{d}_N$), producing physically implausible results, such as transversal velocities pointing upslope and normal velocities indicating uplift, see Sup. B.

We use this constraint to jointly estimate the inter-track datum offset and the unbiased 3D velocities. Taking the descending track as reference[6], a trial offset, $\Delta d^{\text{asc}}_{\text{LoS}}$, is applied to the ascending-track LoS velocities. The strapdown decomposition is recomputed for each trial, and the optimal offset is found by sampling the solution space of possible datum offsets and selecting the

[6]The inter-track datum alignment procedure is independent of the choice of reference track; here, the descending track is used as the reference datum.

one that minimizes the number of negative transversal velocities

$$\min_{\Delta d_{\mathrm{LoS}}^{\mathrm{asc}}} \sum_{i=1}^{n} \mathbf{1}\Big(\hat{d}_{T_i}(d_{\mathrm{LoS},i}^{\mathrm{asc}} + \Delta d_{\mathrm{LoS}}^{\mathrm{asc}}, d_{\mathrm{LoS},i}^{\mathrm{dsc}}) < 0\Big), \tag{1}$$

where $i = 1, \ldots, n$ indexes the RUM observations, $d_{\mathrm{LoS},i}^{\mathrm{asc}}$ and $d_{\mathrm{LoS},i}^{\mathrm{dsc}}$ are the ascending- and descending-track LoS velocities for observation i, $\hat{d}_{T_i}(\cdot)$ is the resulting transversal velocity from the strapdown decomposition given the input LoS velocities, $\Delta d_{\mathrm{LoS}}^{\mathrm{asc}}$ is the trial offset applied to the ascending-track velocities, and $\mathbf{1}(\cdot)$ is an indicator function equal to 1 if the argument is true (i.e., if the transversal velocity is negative) and 0 otherwise.

The optimal offset, $\Delta\hat{d}_{\mathrm{LoS}}^{\mathrm{asc}}$, is determined by sampling the solution space of trial offsets within a pre-defined range, using increments of 0.1 mm yr^{-1} to match InSAR precision (2σ), and then identifying the global minimum analytically. The strapdown decomposition results corresponding to this optimal offset produces physically consistent transversal and normal velocities, $\hat{d}_{T_i}$ and $\hat{d}_{N_i}$, along with their corresponding ENU displacement velocity estimates and variance–covariance matrices in the local datum of the descending InSAR viewing direction.

2.4. InSAR and GNSS datum alignment

Since the decomposed ENU displacement velocities from the strapdown decomposition are expressed in the datum of the descending InSAR track, they must be converted to a terrestrial reference frame for geophysical interpretation. This is achieved using co-located RUMs, defined as RUM cells whose footprint contains at least one GNSS antenna. Within a co-located RUM, the point-like GNSS velocity in the chosen terrestrial reference frame—here the Sunda plate-fixed frame (Bock et al., 2003)—is assumed to represent the same deformation signal as the spatially averaged InSAR velocity obtained from the strapdown decomposition.

For each co-located RUM i, a 3D datum-connection vector is computed as the difference between the GNSS velocity in the Sunda Plate–Fixed Frame, $\hat{d}_i^{\mathrm{G|S}}$, and the RUM-averaged InSAR velocity in the local InSAR datum, $\hat{d}_i^{\mathrm{I}}$

$$\Delta d_i^{\mathrm{I}\to\mathrm{S}} = \hat{d}_i^{\mathrm{G|S}} - \hat{d}_i^{\mathrm{I}}, \tag{2}$$

where $\Delta d_i^{\mathrm{I}\to\mathrm{S}}$ is the 3D offset needed to align the InSAR-derived velocity of RUM i in the local InSAR datum (superscript I) with the corresponding GNSS velocity in the Sunda Plate–Fixed Frame (superscript G|S).

In the general case of multiple co-located RUMs, the final datum-connection vector, $\Delta d^{\mathrm{I}\to\mathrm{S}}$, and its uncertainty are estimated by a least-squares adjustment of all individual datum-connection vectors $\Delta d_i^{\mathrm{I}\to\mathrm{S}}$ derived from the RUM–GNSS pairs. The resulting best-fitting 3D offset is then applied uniformly to the entire InSAR velocity field, thereby connecting it to the chosen terrestrial reference frame. In the present study, the alignment is performed to the Sunda plate-fixed frame (S) using the only existing GNSS station in Jakarta spanning the study period (2014-2025), see Sec. 3. Consequently, the datum-connection vector is the 3D offset computed from a single co-located RUM, and added uniformly to all RUM velocities to express the InSAR-derived field in the Sunda plate-fixed frame

$$\hat{d}_i^{\mathrm{I}|\mathrm{S}} = \hat{d}_i^{\mathrm{I}} + \Delta d^{\mathrm{I}\to\mathrm{S}}. \tag{3}$$

Here, $\hat{d}_i^{\mathrm{I}}$ is the RUM-averaged ENU velocity obtained from the strapdown decomposition in the descending InSAR datum, and $\hat{d}_i^{\mathrm{G}|\mathrm{S}}$ is the ENU GNSS velocity in the Sunda plate-fixed frame. The uncertainties of $\Delta d^{\mathrm{I}\to\mathrm{S}}$ are derived through standard variance propagation, assuming independent uncertainties of the co-located GNSS and RUM-averaged InSAR velocity estimates.

3. Results

To estimate unbiased three-dimensional land motion in Jakarta with associated uncertainties, the ascending-track datum is first aligned to the descending-track datum, establishing a common InSAR datum shared by both tracks. Following the procedure described in Sec. 2.3, a relative datum offset of $\Delta\hat{d}_{\mathrm{LoS}}^{\mathrm{asc}} = 1.2$ mm/yr is estimated by evaluating the objective function in Eq. (1) over all 4779 RUMs, sampling trial offsets within the range $[-2.4, 2.4]$ mm/yr at 0.1 mm/yr increments. The optimal offset corresponds to the unique global minimum of this function, i.e., the minimum number of RUMs exhibiting negative transversal velocities (see supplementary animation rum_bias_animation_sup1.gif). The strapdown decomposition corresponding to the optimal offset $\Delta\hat{d}_{\mathrm{LoS}}^{\mathrm{asc}} = 1.2$ mm/yr yields an unbiased intermediary 3D velocity field of Jakarta expressed in the common InSAR datum.

We connect this intermediary 3D velocity field to the Sunda plate-fixed frame, as described in Sec. 2.4. The 3D datum connection vector is computed at the single co-located RUM containing the CJKT GNSS station. Because only one GNSS station exists that covers the entire duration (2014–2025)

of the study, this vector is directly obtained from the ENU velocity differences between the GNSS velocity (in the Sunda plate-fixed frame) and the co-located RUM velocity from the strapdown decomposition (in the common InSAR datum), following Eq. (2). The final datum connection assumes that the GNSS point velocity represents the same deformation signal as the spatially averaged InSAR velocity of the co-located 450×450 m RUM. Inspection of the original PS LoS velocities within this RUM, see Fig. 3, reveals moderate velocity heterogeneity (range $\approx$ 2.0 mm/yr, σ = 0.5 mm/yr, MAD = 0.4 mm/yr), reflecting the complex urban environment and the presence of multiple scattering mechanisms. Such variability increases the error in estimating the 3D datum offset. To reduce this uncertainty, the co-located RUM is treated conservatively by retaining only LoS velocities from PS in the upper 25% of ellipsoidal heights (above the 75th percentile[7]) prior to the strapdown decomposition, thereby preferentially selecting returns from tall, likely deeply founded structures expected to experience minimal motion, similar to the building hosting the CJKT GNSS antenna, see Fig. 2. As a result, the LoS velocity range—and therefore the potential co-location error—is reduced to 1 mm/yr, ensuring a precise estimation of the datum offset from the single GNSS–InSAR co-location pair.

The estimated 3D datum offset is applied component-wise to the ENU velocity components of all RUMs, transforming the strapdown-derived velocity field into the Sunda plate-fixed frame and yielding the final 3D velocity map shown in Fig. 4. The map shows vertical velocities in color, and directional horizontal (i.e., transversal) velocities with vectors. Only vectors with magnitudes greater than 2σ are plotted, corresponding to a confidence level of at least 95%, so that plotted vectors represent statistically significant motion. Subsidence bowls are clearly visible. Horizontal velocities along the rims of the major subsidence bowls (outlined and numbered in turquoise in Fig. 4) exceed 10 mm/yr, including distinct north components. These horizontal velocity vectors point toward the centers of the subsidence bowls (Kratzsch, 2012), indicating centripetal motion driven by sediment compaction. As pore pressure decreases in unconsolidated sediments, vertical settlement is accompanied by inward horizontal displacement with velocities on the or-

[7]The 75th percentile threshold is chosen pragmatically to select the tallest structures; while somewhat arbitrary, it aims to minimize co-location errors by focusing on points most representative of stable 3D motion.

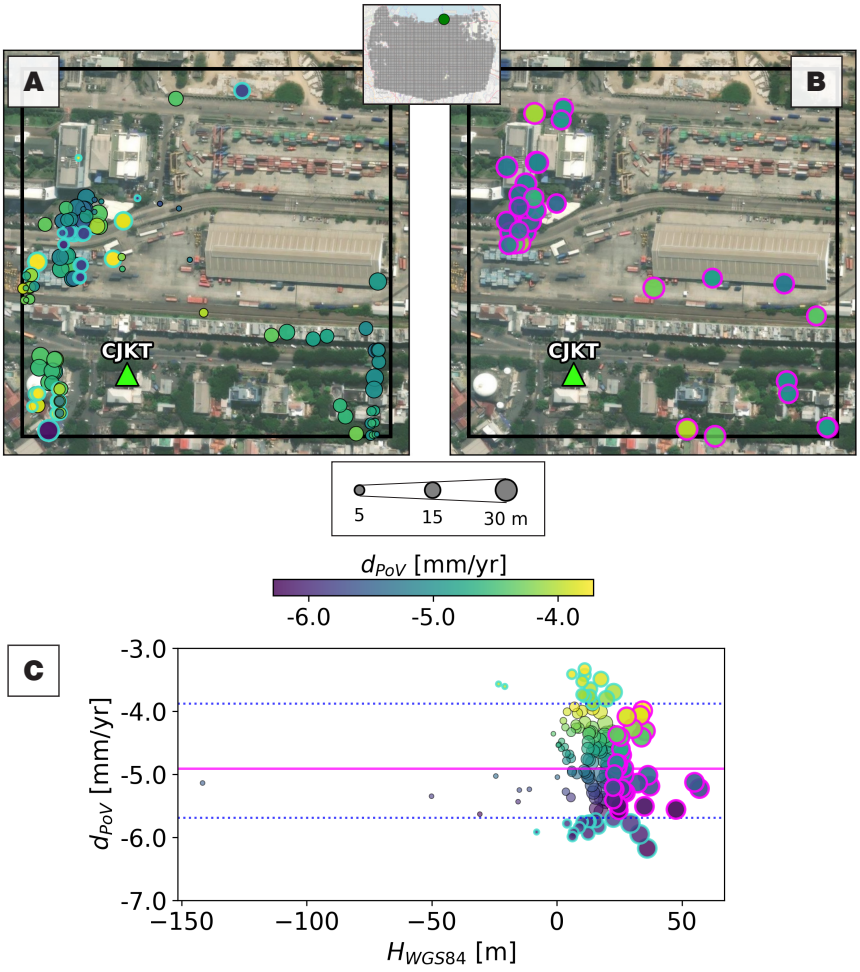

Figure 3: Selection of tall PS within the co-location RUM for precise datum connection to the Sunda plate-fixed frame. Using all PS would alter the estimated datum offset by ~ 0.3 mm/yr. Panels A and B show the 450×450 m co-location RUM (black outline) over satellite imagery, including PS (scatter dots) colored by PoV velocities and the CJKT GNSS station (green triangle). Marker size in all three panels scales with ellipsoidal height (H_{WGS84}). Both track geometries are jointly visualized by first performing the inter-track datum alignment (see Sec. 2.3) and projecting LoS velocities onto the vertical. **A:** *Excluded* PS: lower-elevation points (below the 75th percentile) and points with LoS velocities outside their ±2 MAD interval (turquoise outline). **B:** *Selected* high-elevation PS (magenta outline, highest 25%), used to compute the track-specific RUM-averaged LoS velocities for the strapdown decomposition and estimation of the RUM 3D velocity for datum connection. **C:** PoV velocity versus ellipsoidal height for all PS; dashed blue lines show the ±2 MAD interval computed from all LoS velocities after inter-track datum alignment, and the magenta line shows the median LoS velocity of the selected magenta subset (identical for both tracks). The ±2 MAD interval provides an empirical estimate of potential co-location error (≈ 1 mm/yr).13

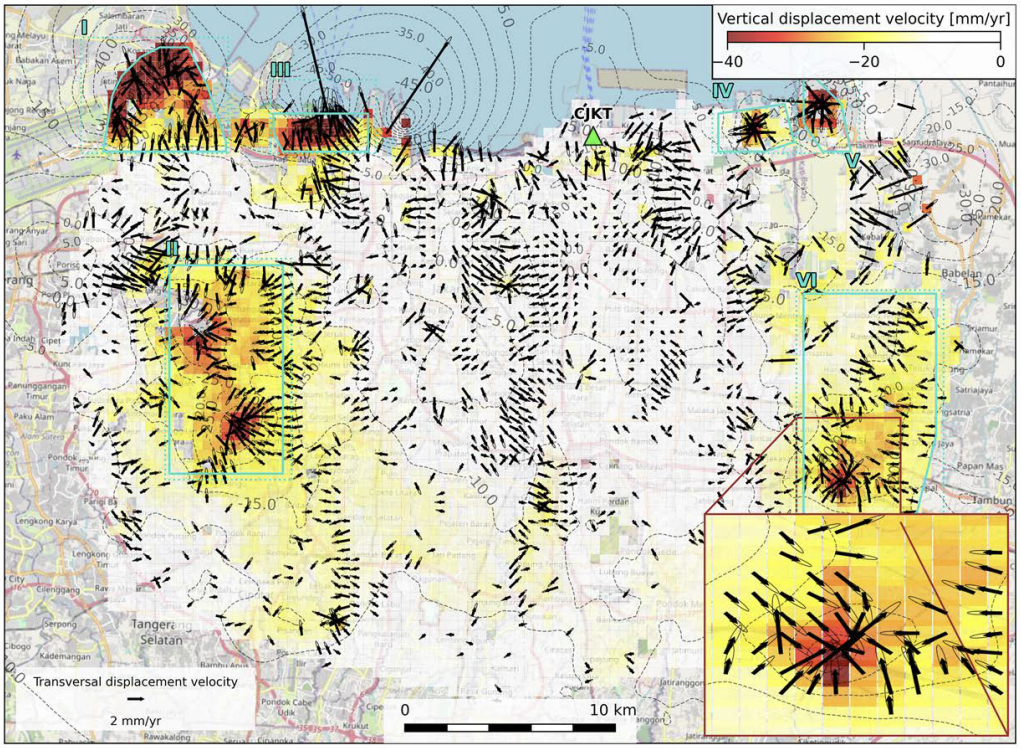

Figure 4: Sunda plate-fixed InSAR velocity map of the Jakarta metropolitan area (2014–2025) obtained via the single-station GNSS (green triangle) based datum connection. Vertical velocities are shown in color, and directional horizontal velocities are shown as vectors with 2σ confidence ellipses; only a subset of the vectors exceeding 2σ are displayed. Six major subsidence bowls (I–VI) are outlined in turquoise, while weaker subsidence patterns below $\sim$ 1 mm/yr (white) may also be present. Directional horizontal velocities near the bowl rims reach up to 10 mm/yr, including distinct north components. Central Jakarta shows little vertical subsidence compared to the bowls. The mean background subsidence rate outside the major bowls is -9.1 mm/yr. The inset in the bottom right corner zooms into Bowl VI, highlighting the centripetal horizontal velocity vectors; for a zoomed-in overview of each bowl see Sup. strapdown_zoomin_bowls.png. The corresponding decomposed 3D ENU velocity components and associated uncertainties are provided in Sup. figures/ENU_field_plot.png

.

der of centimeters per year. This substantial lateral motion may generate shearing along mid-slopes and extensional deformation near the bowl edges, potentially affecting building stability and increasing the vulnerability of underground pipelines.

4. Discussion

4.1. Geophysical discussion

The 3D velocity map in the Sunda plate-fixed frame reveals six spatially localized subsidence bowls, labeled I to VI in Fig. 4 and outlined in turquoise. These bowls exhibit maximum vertical velocities of up to −78.5 mm/yr, and their subsidence characteristics are summarized in Tab. 2. Bowl III in

Bowl #	**# RUMs**	$\hat{d}_{U_i}$ [mm/yr]			$\hat{d}_{T_i}$ [mm/yr]		
		mean	**max**	**max cum. [mm]**	**mean**	**max**	**max cum. [mm]**
I	112	−31.1	−55.9	−594.9	1.5	6.6	69.6
II	275	−21.9	−39.8	−423.4	1.0	3.8	40.4
III	44	−29.7	−78.5	−835.3	2.4	16.9	179.5
IV	32	−15.6	−35.1	−373.9	1.1	4.8	51.1
V	22	−26.0	−51.0	−542.6	2.1	9.8	104.0
VI	358	−17.1	−47.0	−500.2	0.7	5.8	61.7

Table 2: Summary of mean and maximum vertical and directional horizontal (i.e., transversal) subsidence rates and cumulative displacements in Jakarta for each subsidence bowl, based on the CORS-based datum alignment. Velocities are in mm/yr, and cumulative displacements cover a 10.7-year period (October 2014 to June 2025) in mm.

the Muara Angke region shows the strongest deformation, with vertical velocities up to −78.5 mm/yr, a cumulative vertical displacement of −84 cm over the October 2014–June 2025 period, and transversal (i.e., directional horizontal) velocities up to 16.9 mm/yr that may pose risks to utility infrastructure. Bowl I, near Soekarno–Hatta International Airport, also exhibits severe vertical subsidence (maximum −55.9 mm/yr; cumulative −59 cm). The remaining four bowls show substantial but less extreme vertical motion. The six bowls span a variety of urban functions, including industrial areas, residential neighborhoods, commercial districts, and mixed-use zones. In the absence of a clear correlation, subsidence cannot be attributed to specific urban functions. The reported maximum vertical velocities and cumulative displacements are comparable with those of Harintaka et al. (2024), while

about 28% lower than values reported by Sidiq et al. (2025). This difference reflect the methodological steps implemented here, namely the explicit connection to a terrestrial reference frame via inter-track datum alignment and GNSS, and the full 3D displacement decomposition that accounts for horizontal motion.

Several regions along the northern and northeastern coast of Jakarta, represented by the yellow RUMs in Fig. C.7B, exhibit higher intra-RUM velocity variability than the rest of the study area. This is evidenced by larger residual LoS velocities after removal of a planar trend within each RUM, as detailed in Sup. C. These areas correspond to densely built neighborhoods dominated by low-rise structures, likely supported by shallow or absent foundations, which experience slow subsidence with moderate spatial variability and lack the bowl-shaped velocity gradients characteristic of the major subsidence bowls, see Fig. 4. The observed velocity variability therefore points to a different subsidence mechanism, likely related to shallow subsurface mechanisms. Two explanations are plausible: i) localized subsidence due to shallow groundwater extraction, or ii) slow consolidation of young coastal alluvium. Given that these regions are located in districts such as Tanjung Priok, Tambora, Pademangan, and Pluit—where municipal piped-water coverage is high and the phreatic aquifer is polluted (Taftazani et al., 2022)—shallow groundwater pumping is unlikely. Slow consolidation of young coastal alluvium is therefore the more probable mechanism.

Beyond the six subsidence bowls, the entire metropolitan area experiences slow regional subsidence, with a mean vertical velocity of -9.1 mm/yr across Jakarta.

The validity of the geophysical interpretation of Jakarta's subsidence depends on the quality of the final datum connection to the Sunda plate-fixed frame, anchored to the single CORS station at CJKT. As detailed in Sec. 3 and discussed further below, this connection is robust for the study period (2014–2025), with a co-location precision of ~ 1 mm/yr. However, relying on a single GNSS station in a dynamic urban environment has inherent limitations: changes in local building subsidence, or the relocation or destruction of the GNSS monument, could reduce the precision of future datum connections—or even prevent InSAR connection to the Sunda plate-fixed frame entirely. To support reliable long-term monitoring and rigorous InSAR–GNSS alignment, new infrastructure is urgently needed in Jakarta. Establishing multiple Integrated Geodetic Reference Stations (IGRS) (Hanssen, 2017), combining GNSS and corner reflectors visible in multiple InSAR geometries,

would ensure precise ties and consistent alignment of the InSAR datum to the Sunda plate-fixed frame.

4.2. Geodetic discussion

Millimeter-scale misalignments between InSAR LoS datasets from different tracks can propagate through the strapdown decomposition and distort the estimated 3D velocity components. A sensitivity analysis for Jakarta, see Sup. B, shows that neglected inter-track datum offsets may produce biases in both magnitude and direction (including sign flips) of the transversal velocities, whereas normal velocities are affected only about one quarter as much in magnitude and roughly one tenth as much in direction. As the CJKT GNSS station exhibits millimeter-level residual horizontal motion after plate motion removal, see Fig. 2, using GNSS data for inter-track datum alignment would propagate these residuals into the strapdown decomposition, particularly affecting transversal velocities. To avoid introducing such errors from the earliest stage of the decomposition, the methodology in Sec. 2.3 instead exploits the high redundancy[8] of InSAR observations to simultaneously estimate 3D RUM-average velocities and perform inter-track datum alignment with sub-millimeter precision. This alignment is fully independent of GNSS data, providing a physically constrained and internally consistent means to tie multi-track InSAR observations to a common datum. GNSS observations at CJKT are used only for the final connection to the Sunda plate-fixed frame, as described later in this section.

The inter-track datum alignment assumes positive centripetal horizontal motion toward areas of increasing subsidence, a deformation-driven, gravity-compliant assumption in which gravity-driven compaction induces coupled vertical settlement and inward horizontal motion. For Jakarta, this is justified: the study area lies on coastal alluvial soils (Abidin et al., 2015; Colbran, 2009; Nugraha et al., 2024) with no known active faults crossing it, and the southward-dipping Baribis Fault (Gunawan et al., 2025), 50 km to the north, is too distant and oriented away to produce significant tectonic uplift or centrifugal horizontal motion. Consequently, the observed inward horizontal motion toward the centers of subsidence bowls is consistent with compaction-driven subsidence, likely linked to groundwater extraction (Kratzsch, 2012).

[8] $>$ 50 PS per RUM per track across all 4779 RUMs

The success of the strapdown decomposition in Jakarta relies on a spatially coherent deformation regime, where the velocity change along iso-displacement lines is zero and strong radial gradients across subsidence bowls define the local TLN orientation, enabling accurate 3D velocity reconstruction. To verify this spatial coherence across the metropolitan area, a planar trend is fitted to the LoS velocities within each RUM, see Sup. C. Most areas (88% of RUMs) show low residuals and semi-variance after planar removal, with the strongest reduction within the six major subsidence bowls, see Fig. C.7, indicating that deep-seated, long-wavelength compaction dominates Jakarta's primary subsidence signal. By contrast, a small subset of RUMs (yellow in Fig. C.7B) retains higher residual variability. Here, PS elevations vary by only $\sim$ 20 m (2σ) and LoS velocity differences remain within $\pm$3.5 mm/yr, indicating that this variability is not elevation-dependent. These regions are characterized by slow subsidence, weak velocity gradients, and less well resolved horizontal motion. This pattern suggests a different subsidence mechanism than in the main bowls, most likely related to shallow subsurface processes such as consolidation of young coastal alluvium, as discussed in the geophysical context.

In the final step, the strapdown-derived 3D velocity field is aligned to the Sunda plate-fixed frame using the CORS station at CJKT, the only long-term GNSS infrastructure available for datum connection in Jakarta, as confirmed by national geospatial authorities[9]. The alignment assumes that highly elevated PS within the co-located RUM—associated with tall, deeply founded structures—exhibit minimal motion, similar to the building hosting the GNSS monument. Careful selection and evaluation of these PS ensure a representative RUM velocity, yielding a co-location precision of $\sim$ 1 mm/yr for the 2014–2025 period, see Fig. 3, within which this assumption is valid. While this supports a reliable datum connection for the study period, long-term reliability is not guaranteed, as future differential settlement or modifications to the structures hosting the selected PS in the co-location RUM or the GNSS monument may degrade or prevent the datum connection. Ensuring consistent, long-term alignment of InSAR-derived 3D velocity products to the Sunda plate-fixed frame will therefore require establishing multiple co-located GNSS–InSAR benchmarks across Jakarta.

[9]Badan Informasi Geospasial (BIG) and Jakarta Survey Division

5. Conclusion

Three-dimensional displacement velocities for Jakarta are estimated on a 450 × 450 m grid covering 2014–2025 and referenced to the Sunda plate-fixed frame, achieving sub-millimeter precision that resolves detailed subsidence patterns beyond the capability of traditional GNSS or leveling surveys. All estimates are accompanied by a full variance–covariance matrix, allowing detailed analysis of displacement significance for applications such as groundwater management and flood-risk assessment, supporting city planning and asset management.

Unlike previous InSAR studies relying on simplified geometric decompositions, this study produces the first unbiased 3D velocity field for Jakarta, including the often neglected north component. The velocity field shows that Jakarta's land motion is dominated by six distinct subsidence bowls with extreme localized displacement (maximum vertical velocity -77.4 mm/yr), superimposed on slower regional subsidence, with a mean background vertical velocity of -9.1 mm/yr across the metropolitan area, calculated outside the major bowls. Several smaller coastal areas along the northern and northeastern shores exhibit slower, spatially heterogeneous subsidence without the characteristic bowl-shaped gradients, providing the first spatial evidence of multiple coexisting subsidence processes in Jakarta, likely reflecting natural consolidation of young coastal alluvium. Localized directional horizontal displacements of up to 17 mm/yr are observed, providing statistically significant information for assessing deformation pathways and infrastructure risk.

Currently, the InSAR 3D velocity field is tied to the Sunda plate-fixed frame via the single long-term CORS GNSS station at CJKT, the only such infrastructure available in Jakarta. Careful selection of high-elevation point scatterers within a region co-located with the CJKT GNSS station ensures that the InSAR line-of-sight and GNSS velocities capture the same deformation signal, providing a reliable datum connection for 2014–2025 with $\sim$ 1 mm/yr precision. Although robust over this period, long-term reliability of the datum connection could be affected by settlement or changes to the structures hosting the point scatterers or the GNSS monument. To ensure continued, accurate alignment of InSAR-derived 3D velocities to the Sunda plate-fixed frame, deploying and maintaining multiple co-located GNSS–InSAR benchmarks across Jakarta is imperative for long-term monitoring of land subsidence and safeguarding coastal and urban resilience.

The findings demonstrate a novel procedure that combines strapdown

decomposition of ascending and descending InSAR displacement velocities, a deformation-driven internal datum connection, and a GNSS-based InSAR datum alignment to a global terrestrial reference frame. This approach provides a comprehensive 3D subsidence monitoring method for Jakarta and establishes a transferable framework for other rapidly subsiding megacities, emphasizing that careful InSAR datum alignment is as critical as the subsidence measurements themselves.

Supplementary material

Supplementary material is available for this article. In this review version, the appendices are included directly in the manuscript to provide reviewers with easy access to the supporting information; in the final version, these appendices are intended to form part of the supplementary material. In addition to the textual appendices, the supplementary material also includes a supplementary animation illustrating the iterative estimation of the inter-track datum offset, $\Delta\hat{d}^{\mathrm{asc}}_{\mathrm{LoS}}$, described in Sec. 2.3, as well as two additional figures containing input line-of-sight observations and zoomed bowl-scale visualizations. All supplementary items should be considered supporting information to the main article.

Acknowledgements

We thank Dr. F. van Leijen for valuable input on selecting InSAR processing parameters in DePSI. We also thank Bayu Triyogo Widyantoro, Sidik Tri Wibowo, and Febrylian Fahmi Chabibi from Badan Informasi Geospasial (BIG) for providing the GNSS data of the CORS station at CJKT in RINEX format.

Funding

This work was supported by the Dutch Research Council (NWO) through the Three SISTERS (grant no: NWO-WOTRO-482.21.505) project and by the Merian Fund Southeast Asia–Europe Joint Funding Scheme.

Declaration of Competing Interest

The authors declare that they have no known competing financial interests or personal relationships that could have appeared to influence the work reported in this paper.

Data availability

The final 3D ground displacement velocity estimates (east, north, up) for the Jakarta city and metropolitan area, including variance-covariance values are available at https://doi.org/10.4121/39e7a39c-d305-425f-b238-1f3a4271dda9. The North–East–Up GNSS time series of the CJKT CORS station are available from the Zenodo repository at https://doi.org/10.5281/zenodo.7775016 (Susilo et al., 2023).

All other data and materials required to evaluate the conclusions of this study are included in the article and the supplementary material.

Author Contributions

A.M.L. contributed to Conceptualization, Methodology, Formal analysis, Investigation, Data Curation, Visualization, and Writing – Original Draft; designed the research, performed the analysis, created the figures, and wrote the first draft. H.A. contributed to Investigation, Resources, Data Curation, and Writing – Review & Editing; conducted, processed, and provided the GNSS data and additional metadata on the GNSS benchmarks. D.P. contributed to Investigation, Resources, and Data Curation; conducted, processed, and provided the GNSS data and additional metadata on the GNSS benchmarks. W.B. contributed to Methodology and Software; developed the strapdown method and provided feedback on its application. S.v.D. contributed to Investigation and Data Curation; processed the InSAR data. R.H. contributed to Supervision and Writing – Review & Editing; analyzed, reviewed, and edited the manuscript.

A. Mathematical Formulation of Strapdown Decomposition

The strapdown decomposition is used to estimate 3D displacement velocities from InSAR LoS velocity observations, following the approach of Brouwer and Hanssen (2024).

Let the vector of unknown parameters for each RUM be

$$x = [d_T, d_L, d_N, \Lambda, \Omega, \Phi]^T, \tag{A.1}$$

where d_T, d_L, d_N are the displacement velocities in the transversal, longitudinal (along the iso-displacement contour lines), and normal directions of the local TLN coordinate system, and Λ, Ω, Φ are the orientation angles of the TLN coordinate system, treated as pseudo-observation representing prior approximations for the TLN frame orientation.

The observations used to estimate these RUM-specific parameters are organized into $s = 1, \ldots, m$ sets, each corresponding to a distinct SAR viewing geometry (ascending or descending). These observations consist of RUM-averaged LoS velocities for each SAR viewing geometry and the pre-set TLN orientation angles, related to the unknowns through

$$E\{\begin{bmatrix} \underline{d}_{\text{LoS}}^{(1)} \\ \vdots \\ \underline{d}_{\text{LoS}}^{(m)} \\ \underline{\Lambda} \\ \underline{\Omega} \\ \underline{\Phi} \end{bmatrix}\} = \begin{bmatrix} a_1(x) \\ \vdots \\ a_m(x) \\ \Lambda \\ \Omega \\ \Phi \end{bmatrix}, \quad a_s(x) = P_T^{(s)}(\Lambda, \Omega, \Phi) d_T + P_L^{(s)}(\Lambda, \Omega, \Phi) d_L + P_N^{(s)}(\Lambda, \Omega, \Phi) d_N, \tag{A.2}$$

where $P_T^{(s)}, P_L^{(s)}, P_N^{(s)}$ project the TLN velocities onto the LoS for all observations in set s.

For Jakarta, each RUM has two sets, corresponding to Sentinel-1 ascending track 98 and descending track 47. In the equations of the main text, the set index is indicated as a superscript: $s = \text{asc}$ for the ascending track and $s = \text{dsc}$ for the descending track. The RUM-averaged LoS velocity observations are computed as the robust median of all PS within each RUM (see Sec. 2.2) and, together with the pre-set TLN angles Φ and Ω (set to 0) and the longitudinal azimuth Λ initialized from the 2D gradient of PoV velocities, are used to estimate the RUM-specific 3D displacement velocity parameters.

The dispersion of the observations is described by the covariance matrix

$$D\{\begin{bmatrix} \underline{d}_{\mathrm{LoS}}^{(1)} \\ \vdots \\ \underline{d}_{\mathrm{LoS}}^{(m)} \\ \underline{\Lambda} \\ \underline{\Omega} \\ \underline{\Phi} \end{bmatrix}\} = \begin{bmatrix} Q_{\mathrm{LoS},1} & 0 & \cdots & 0 & 0 & 0 & 0 \\ 0 & Q_{\mathrm{LoS},2} & \cdots & 0 & 0 & 0 & 0 \\ \vdots & \vdots & \ddots & \vdots & \vdots & \vdots & \vdots \\ 0 & 0 & \cdots & Q_{\mathrm{LoS},m} & 0 & 0 & 0 \\ 0 & 0 & \cdots & 0 & \sigma_\Lambda^2 & 0 & 0 \\ 0 & 0 & \cdots & 0 & 0 & \sigma_\Omega^2 & 0 \\ 0 & 0 & \cdots & 0 & 0 & 0 & \sigma_\Phi^2 \end{bmatrix}, \tag{A.3}$$

where $Q_{\mathrm{LoS},s}$ is the variance–covariance matrix of the RUM-averaged LoS observation in set s, derived via standard error propagation for the median averaging, and σ_Λ^2, σ_Ω^2, and σ_Φ^2 are the variances of the TLN pseudo-observation angles. For Jakarta, these are pre-set to $\sigma_\Lambda = 10^\circ$ and $\sigma_\Omega = \sigma_\Phi = 3^\circ$ (see Sec. 2.3).

The displacement velocity vector from x, $d_{\mathrm{TLN}} = [d_T, d_L, d_N]^T$, is projected onto the LoS direction via a projection onto the plane orthogonal to the LoS, using the projector

$$P_{\mathrm{LoS}^\perp}^R = [P_T, P_L, P_N], \tag{A.4}$$

with components

$$\begin{aligned} P_T = {} & (\sin\theta \sin\alpha_d \cos\Lambda - \sin\theta \cos\alpha_d \sin\Lambda)\cos\Omega \\ & - \Big((-\sin\theta \sin\alpha_d \sin\Lambda + \sin\theta \cos\alpha_d \cos\Lambda)\sin\Phi \\ & + \cos\theta \cos\Phi\Big)\sin\Omega, \end{aligned} \tag{A.5}$$

$$\begin{aligned} P_L = {} & (\sin\theta \sin\alpha_d \sin\Lambda + \sin\theta \cos\alpha_d \cos\Lambda)\cos\Phi \\ & + \cos\theta \sin\Phi, \end{aligned} \tag{A.6}$$

$$\begin{aligned} P_N = {} & (\sin\theta \sin\alpha_d \cos\Lambda - \sin\theta \cos\alpha_d \sin\Lambda)\sin\Omega \\ & + \Big((-\sin\theta \sin\alpha_d \sin\Lambda + \sin\theta \cos\alpha_d \cos\Lambda)\sin\Phi \\ & + \cos\theta \cos\Phi\Big)\cos\Omega. \end{aligned} \tag{A.7}$$

Here, θ denotes the incidence angle toward the radar, and α_d is the azimuth of the zero-Doppler plane at the target location, measured in the direction toward the satellite (Brouwer and Hanssen, 2023).

The unknown parameter vector x in Eq. (A.1) is estimated using an iterative Gauss–Newton approach applied to the observation model in Eq. (A.2).

At each iteration, the nonlinear equations are linearized around the current estimate and solved in a weighted least-squares sense until convergence is reached, yielding the final parameter estimates $\hat{x}$ and their associated covariance matrix $Q_{\hat{x}}$. The latter can be written in block-diagonal form as $Q_{\hat{x}} = \mathrm{blockdiag}\big(Q_{\hat{\underline{d}}_{\mathrm{TLN}}}, Q_{\hat{\underline{\Lambda}}}, Q_{\hat{\underline{\Omega}}}, Q_{\hat{\underline{\Phi}}}\big)$.

The estimated TLN displacement velocities $\hat{\underline{d}}_{\mathrm{TLN}} = [\hat{\underline{d}}_T, \hat{\underline{d}}_L, \hat{\underline{d}}_N]^T$ and their covariance matrix $Q_{\hat{\underline{d}}_{\mathrm{TLN}}}$ are subsequently rotated into the local East–North–Up (ENU) coordinate system using the estimated orientation angles $\hat{\underline{\Lambda}}$, $\hat{\underline{\Omega}}$, and $\hat{\underline{\Phi}}$

$$\mathbf{R}_{\mathrm{TLN}\to\mathrm{ENU}} = \mathbf{R}_{\hat{\underline{\Lambda}}}\, \mathbf{R}_{\hat{\underline{\Omega}}}\, \mathbf{R}_{\hat{\underline{\Phi}}}, \tag{A.8}$$

$$\mathbf{R}_{\hat{\underline{\Lambda}}} = \begin{bmatrix} \cos\hat{\underline{\Lambda}} & \sin\hat{\underline{\Lambda}} & 0 \\ -\sin\hat{\underline{\Lambda}} & \cos\hat{\underline{\Lambda}} & 0 \\ 0 & 0 & 1 \end{bmatrix}, \quad \mathbf{R}_{\hat{\underline{\Omega}}} = \begin{bmatrix} \cos\hat{\underline{\Omega}} & 0 & \sin\hat{\underline{\Omega}} \\ 0 & 1 & 0 \\ -\sin\hat{\underline{\Omega}} & 0 & \cos\hat{\underline{\Omega}} \end{bmatrix}, \quad \mathbf{R}_{\hat{\underline{\Phi}}} = \begin{bmatrix} 1 & 0 & 0 \\ 0 & \cos\hat{\underline{\Phi}} & \sin\hat{\underline{\Phi}} \\ 0 & -\sin\hat{\underline{\Phi}} & \cos\hat{\underline{\Phi}} \end{bmatrix}. \tag{A.9}$$

The ENU displacement velocities are obtained by rotating the estimated TLN velocities using $\mathbf{R}_{\mathrm{TLN}\to\mathrm{ENU}}$, i.e., $\hat{\underline{d}}_{\mathrm{ENU}} = \mathbf{R}_{\mathrm{TLN}\to\mathrm{ENU}}\, \hat{\underline{d}}_{\mathrm{TLN}}$, while the associated covariance matrix is propagated as $Q_{\hat{\underline{d}}_{\mathrm{ENU}}} = \mathbf{R}_{\mathrm{TLN}\to\mathrm{ENU}}\, Q_{\hat{\underline{d}}_{\mathrm{TLN}}}\, \mathbf{R}_{\mathrm{TLN}\to\mathrm{ENU}}^{\top}$, yielding the final 3D displacement components in the ENU coordinate system together with their full variance–covariance information.

For a full description of the equations and the estimation procedure, see Brouwer and Hanssen (2024).

B. Effect of inter-track datum misalignment on the relative velocity map of Jakarta

To quantify the impact of datum misalignment on the decomposed 3D velocity field, we compute both magnitude and directional (sign flip) residuals between the unaligned ($\Delta d^{\text{asc}}_{\text{LoS}} = 0$ mm/yr) and aligned ($\Delta \hat{d}^{\text{asc}}_{\text{LoS}} = 1.2$ mm/yr) decomposed velocity fields of each RUM, after the inter-track datum alignment, see Sec. 2.3. Magnitude residuals are defined as

$$\begin{aligned} \Delta \hat{d}_{T_i} &= \hat{d}_{T_i}\big(d^{\text{asc}}_{\text{LoS}_i}, d^{\text{dsc}}_{\text{LoS}_i}\big) - \hat{d}_{T_i}\big(d^{\text{asc}}_{\text{LoS}_i} + \Delta d^{\text{asc}}_{\text{LoS}_i}, d^{\text{dsc}}_{\text{LoS}_i}\big), \\ \Delta \hat{d}_{N_i} &= \hat{d}_{N_i}\big(d^{\text{asc}}_{\text{LoS}_i}, d^{\text{dsc}}_{\text{LoS}_i}\big) - \hat{d}_{N_i}\big(d^{\text{asc}}_{\text{LoS}_i} + \Delta d^{\text{asc}}_{\text{LoS}_i}, d^{\text{dsc}}_{\text{LoS}_i}\big). \end{aligned} \tag{B.1}$$

The magnitude bias is expressed as the Weighted Mean Absolute Bias (WMAB):

$$\begin{aligned} \text{WMAB}_T &= \frac{1}{n}\sum_{i=1}^{n} \big|\Delta \hat{d}_{T_i}\big|, \\ \text{WMAB}_N &= \frac{1}{n}\sum_{i=1}^{n} \big|\Delta \hat{d}_{N_i}\big|. \end{aligned} \tag{B.2}$$

Directional bias is quantified as the percentage of RUMs exhibiting a sign flip

$$\begin{aligned} \Delta\theta_T &= \frac{100}{n}\sum_{i=1}^{n} \mathbb{1}\Big(\hat{d}_{T_i}\big(d^{\text{asc}}_{\text{LoS}_i}, d^{\text{dsc}}_{\text{LoS}_i}\big) \cdot \hat{d}_{T_i}\big(d^{\text{asc}}_{\text{LoS}_i} + \Delta d^{\text{asc}}_{\text{LoS}_i}, d^{\text{dsc}}_{\text{LoS}_i}\big) < 0\Big), \\ \Delta\theta_N &= \frac{100}{n}\sum_{i=1}^{n} \mathbb{1}\Big(\hat{d}_{N_i}\big(d^{\text{asc}}_{\text{LoS}_i}, d^{\text{dsc}}_{\text{LoS}_i}\big) \cdot \hat{d}_{N_i}\big(d^{\text{asc}}_{\text{LoS}_i} + \Delta d^{\text{asc}}_{\text{LoS}_i}, d^{\text{dsc}}_{\text{LoS}_i}\big) < 0\Big), \end{aligned} \tag{B.3}$$

where $\mathbb{1}(\cdot)$ is the indicator function, which equals 1 if the argument is true (i.e., if the unaligned decomposed velocity has the opposite sign to the aligned decomposed velocity for the same RUM, their product will be negative) and 0 otherwise. For transversal velocities, the positive direction is defined as downslope (centripetal), while normal velocities are expected to be negative in sinking regions.

Fig. B.5 compares the unaligned and aligned decomposed velocities over the entire RUM field. Transversal velocities show a magnitude bias of $\text{WMAB}_T = 6.86$ mm/yr and directional flips $\Delta\theta_T = 33\%$, whereas normal velocities show smaller biases: $\text{WMAB}_N = 1.51$ mm/yr and $\Delta\theta_N = 2\%$.

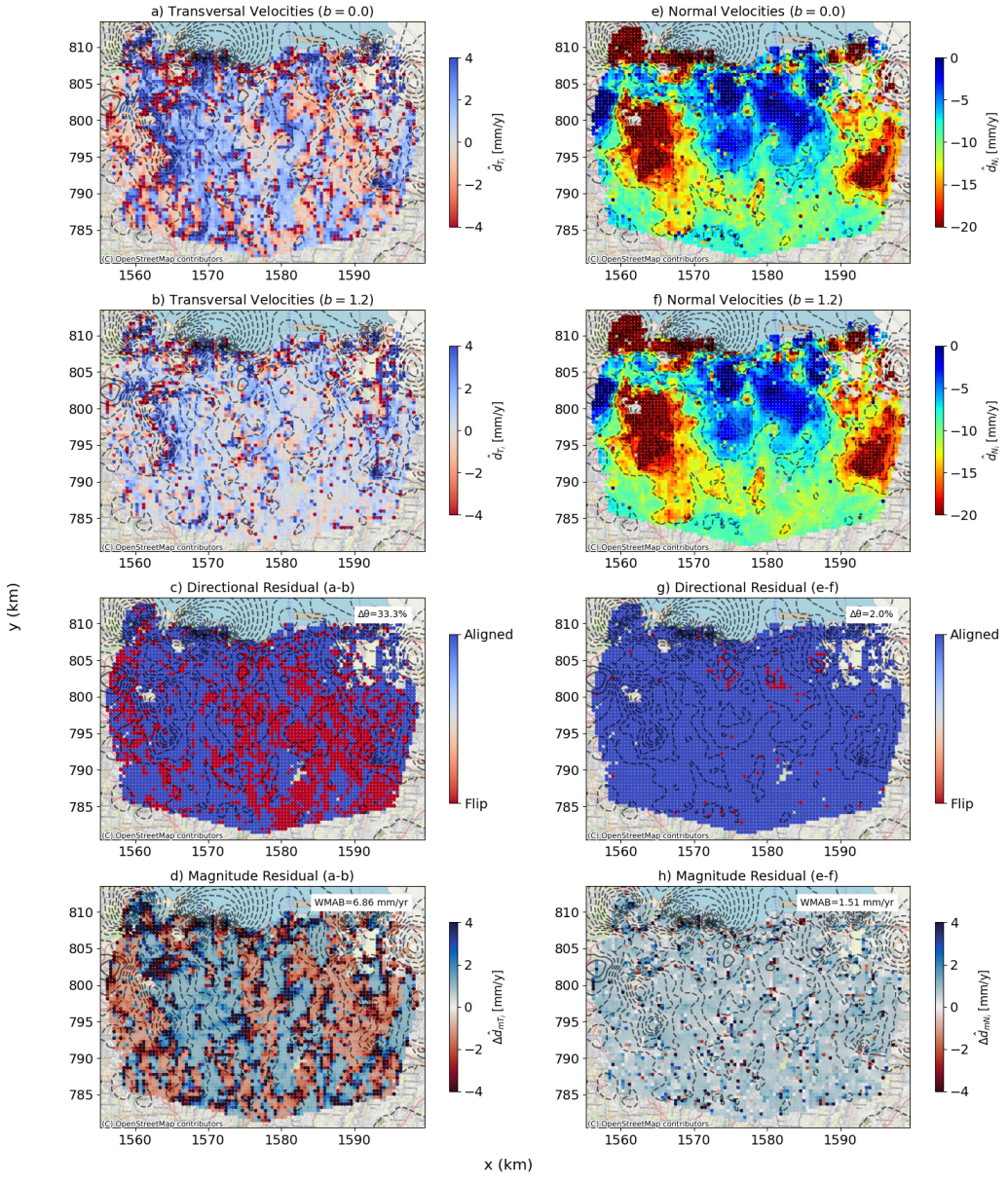

Figure B.5: Directional and magnitude biases due to inter-track datum misalignment in Jakarta. Columns show transversal (first) and normal (second) velocity components. Panels (a)–(b) compare unaligned ($\Delta d^{\text{asc}}_{\text{LoS}} = 0.0\,\text{mm/yr}$) and aligned ($\Delta d^{\text{asc}}_{\text{LoS}} = 1.2\,\text{mm/yr}$) transversal velocities; panels (e)–(f) show the same for normal velocities. Panels (c)–(d) and (g)–(h) display spatial variability of directional and magnitude biases.

Fig. B.6 shows the effect of varying the ascending track datum offset, $\Delta d_{\mathrm{LoS}}^{\mathrm{asc}}$, from -2.2 to $+2.2$ mm/yr in steps of 0.1 mm/yr. Transversal velocities reach up to 20 mm/yr (WMAB) and 45% directional flips, while normal velocities reach up to 4.8 mm/yr and 5% flips. Both magnitude and directional biases show a clear minimum at $\Delta d_{\mathrm{LoS}}^{\mathrm{asc}} = 1.2$ mm/yr, highlighting the necessity of proper datum alignment.

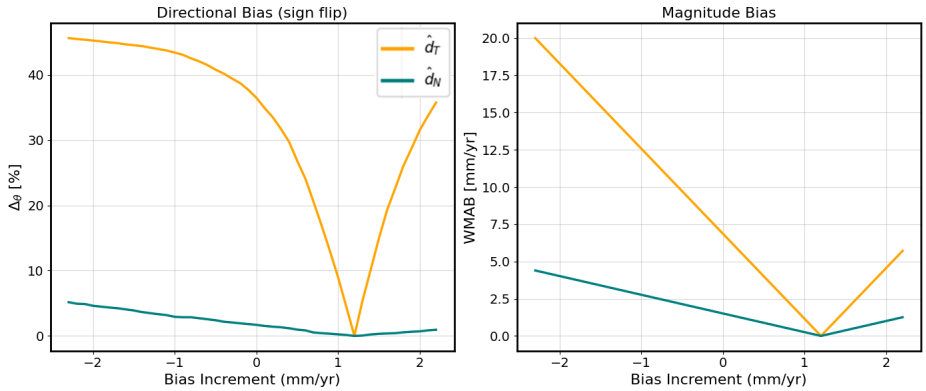

Figure B.6: Directional bias ($\Delta\theta$, left) and magnitude bias (WMAB, right) for transversal (T, orange) and normal (N, blue) velocity components across inter-track datum offsets. Transversal velocities are more sensitive, reaching 20 mm/yr (WMAB) and 45% ($\Delta\theta$). Both curves show a minimum at $\Delta d_{\mathrm{LoS}}^{\mathrm{asc}} = 1.2$ mm/yr.

C. Inter-RUM LoS velocity homogeneity assessment

Fig. C.7 evaluates intra-RUM LoS velocity homogeneity for the ascending and descending tracks to determine whether the estimated 3D velocity field of Jakarta (Fig. 4) reflects a spatially coherent subsidence regime. Within each RUM, homogeneity was assessed using the standard deviation of LoS velocities, the standard deviation and the semi-varianve $\gamma(h)$ of residual velocities after planar detrending. The semi-variance lag was set to $h \approx 60$ m, determined by first computing the mean nearest-neighbor distance d_{nn} between PS points ($\sim$ 11 m ascending, $\sim$ 9.5 m descending) and then incrementally evaluating the scale-dependent heterogeneity $H(n) = \gamma(n\, d_{\mathrm{nn}})/\sigma^2$ for increasing multiples n until the critical lag n_{crit} is reached. The critical lag n_{crit} is defined as the smallest n for which $H > 1$, indicating that local residual velocity variability exceeds the total RUM variance.

RUM velocities are considered spatially uniform—and therefore dominated by homogeneous, long-wavelength subsidence—if the LoS velocities are well described by a planar fit, with small residuals ($\sigma < 1$ mm/yr) and low semi-variance ($\gamma < 0.8$ mm^2/yr^2). Approximately 88% of RUMs meet these criteria, especially within the six major subsidence bowls, highlighting areas dominated by deep-seated, long-wavelength compaction. In contrast, a small subset of RUMs along the northern and northeastern coasts (yellow regions in Fig. C.7B), including Tanjung Priok, Tambora, Pademangan, Pluit, and a north-south feature from Muara Baru to Central Jakarta, exhibits higher residual variability and semi-variance. These areas are less spatially coherent and likely reflect different, shallower or more localized subsidence mechanisms, making the 3D velocity estimates there less well constrained.

References

Abdullah, F.M., Andriyanto, H., Nababan, J.R., Abdillah, F., Sulistyawan, R.I.H., 2021. Results of Land Subsidence Measurement using GPS Method in the Jakarta Groundwater Basin in 2015–2019, in: IOP Conference Series: Earth and Environmental Science, p. 012034. doi:`https://doi.org/10.1088/1755-1315/873/1/012034`.

Abidin, H., Djaja, R., Andreas, H., Gamal, M., Hirose, K., Maruyama, Y., 2004. Capabilities and Constraints of Geodetic Techniques for Monitoring Land Subsidence in the Urban Areas of Indonesia. Geomatics Research Australia 81, 45–58.

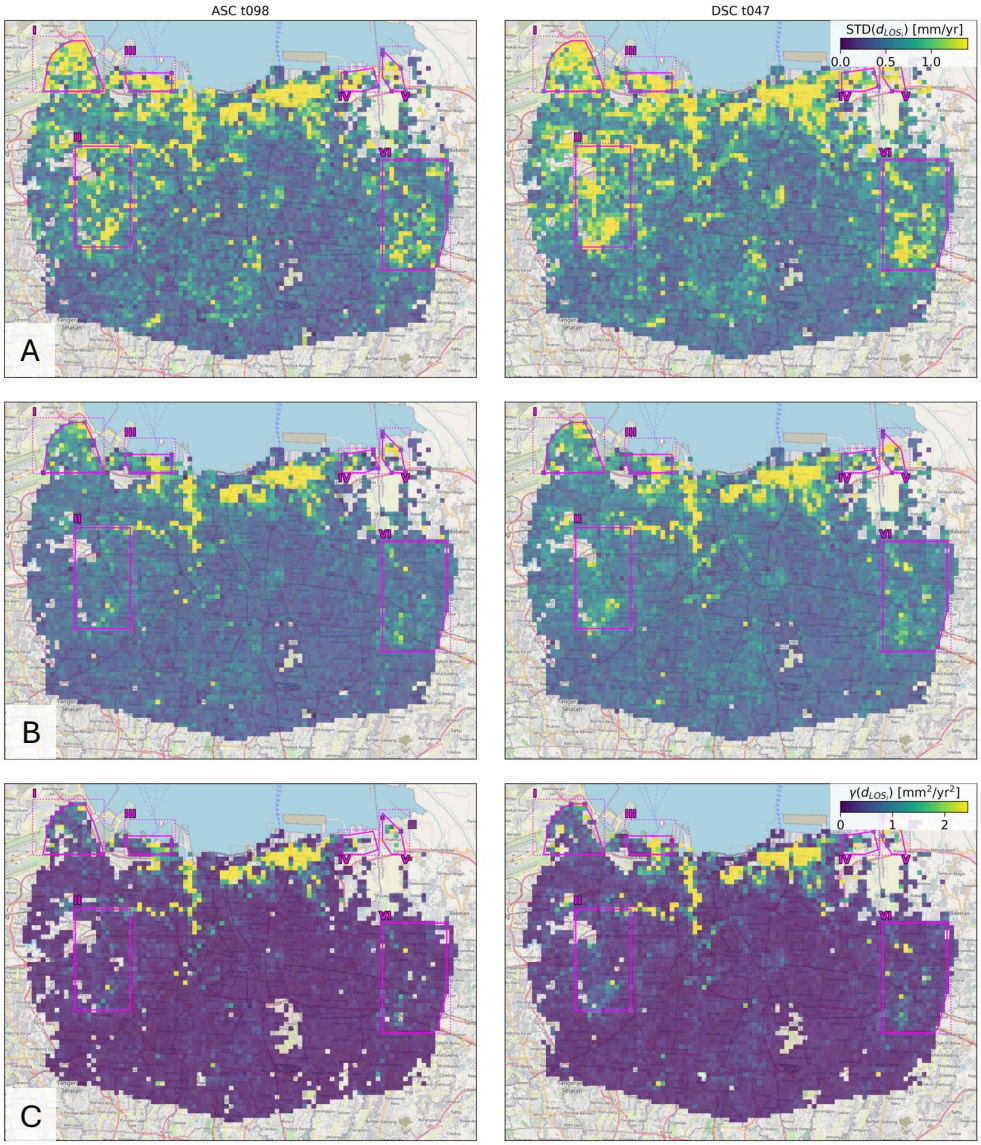

Figure C.7: Inter-RUM LoS velocity variability assessment. The six major subsidence bowls (outlined in turquoise in Fig. 4) are highlighted in magenta. **Row A:** Standard deviation of original ascending (left) and descending (right) LoS velocities at the RUM level. **Row B:** Standard deviation of residual velocities after removing a planar trend within each RUM. After plane removal, 88% of RUMs have $\sigma < 1$ mm/yr, with the largest reductions in the subsidence bowls, indicating long-wavelength, spatially coherent motion. **Row C:** Semi-variance of residual velocities computed at a distance lag of $h \approx 60$ m, showing spatial correlation at short distances. Again, 88% of the AOI exhibits low semi-variance ($\gamma < 0.8$ mm^2/yr^2), while northeastern and northern coastal regions (yellow) retain higher residuals, suggesting subsidence there is not dominated by a uniform, deep-seated mechanism.

Abidin, H.Z., Andreas, H., Djaja, R., Darmawan, D., Gamal, M., 2008. Land Subsidence Characteristics of Jakarta between 1997 and 2005, as estimated using GPS Surveys. GPS Solutions 12, 23–32. doi:https://doi.org/10.1007/s10291-007-0061-0.

Abidin, H.Z., Andreas, H., Gamal, M., Djaja, R., Subarya, C., Hirose, K., Maruyama, Y., Murdohardono, D., Rajiyowiryono, H., 2005. Monitoring Land Subsidence of Jakarta (Indonesia) using Leveling, GPS Survey and InSAR Techniques, in: A Window on the Future of Geodesy: Proceedings of the International Association of Geodesy IAG General Assembly, Sapporo, Japan, June 30–July 11, 2003, pp. 561–566. doi:https://doi.org/10.1007/3-540-27432-4_95.

Abidin, H.Z., Andreas, H., Gumilar, I., Brinkman, J.J., 2015. Study on the Risk and Impacts of Land Subsidence in Jakarta. Proceedings of the International Association of Hydrological Sciences 372, 115–120. doi:https://doi.org/10.5194/piahs-372-115-2015.

Abidin, H.Z., Andreas, H., Gumilar, I., Fukuda, Y., Pohan, Y.E., Deguchi, T., 2011. Land Subsidence of Jakarta (Indonesia) and its Relation with Urban Development. Natural Hazards 59, 1753–1771. doi:https://doi.org/10.1007/s11069-011-9866-9.

Abidin, H.Z., Andreas, H., Gumilar, I., Sidiq, T.P., Pradipta, D., Yuwono, B.D., 2022. On the Disaster Risk Reduction of Land Subsidence in Indonesia's Northern Coastal Areas of Java, in: EGU General Assembly Conference Abstracts, pp. EGU22–1721. doi:https://doi.org/10.13140/RG.2.2.34300.00646.

Abidin, H.Z., Djaja, R., Darmawan, D., Hadi, S., Akbar, A., Rajiyowiryono, H., Sudibyo, Y., Meilano, I., Kasuma, M.A., Kahar, J., 2001. Land Subsidence of Jakarta (Indonesia) and its Geodetic Monitoring System. Natural Hazards 23, 365–387.

Batubara, B., Kooy, M., Zwarteveen, M., 2023. Politicising Land Subsidence in Jakarta: How Land Subsidence is the Outcome of uneven Sociospatial and Socionatural Processes of Capitalist Urbanization. Geoforum 139, 1–9.

Bennett, W.G., Karunarathna, H., Xuan, Y., Kusuma, M.S., Farid, M., Kuntoro, A.A., Rahayu, H.P., Kombaitan, B., Septiadi, D., Kesuma, T.N.,

et al., 2023. Modelling Compound Flooding: A Case Study from Jakarta, Indonesia. Natural Hazards 118, 277–305. doi:https://doi.org/10.1007/s11069-023-06001-1.

Berardino, P., Fornaro, G., Lanari, R., Sansosti, E., 2003. A new Algorithm for Surface Deformation Monitoring based on Small Baseline Differential SAR Interferograms. IEEE Transactions on Geoscience and Remote Sensing 40, 2375–2383. doi:https://doi.org/10.1109/TGRS.2002.803792.

Bock, Y., Prawirodirdjo, L., Genrich, J.F., Stevens, C.W., McCaffrey, R., Subarya, C., Puntodewo, S.S.O., Calais, E., 2003. Crustal Motion in Indonesia from Global Positioning System Measurements. Journal of Geophysical Research: Solid Earth 108. doi:https://doi.org/10.1029/2001JB000324.

Brouwer, W.S., Hanssen, R.F., 2021. An Analysis of InSAR Displacement Vector Decomposition Fallacies and the Strap-Down Solution, in: 2021 IEEE International Geoscience and Remote Sensing Symposium (IGARSS), pp. 2927–2930.

Brouwer, W.S., Hanssen, R.F., 2023. A Treatise on InSAR Geometry and 3-D Displacement Estimation. IEEE Transactions on Geoscience and Remote Sensing 61, 1–11. doi:https://doi.org/10.1109/TGRS.2023.3322595.

Brouwer, W.S., Hanssen, R.F., 2024. Estimating Three-Dimensional Displacements with InSAR: The Strapdown Approach. Journal of Geodesy 98, 110.

Chang, L., Dollevoet, R.P., Hanssen, R.F., 2018. Monitoring line-infrastructure with multisensor sar interferometry: products and performance assessment metrics. IEEE journal of selected topics in applied earth observations and remote sensing 11, 1593–1605.

Chaussard, E., Amelung, F., Abidin, H., Hong, S.H., 2013. Sinking Cities in Indonesia: ALOS PALSAR detects rapid Subsidence due to Groundwater and Gas Extraction. Remote Sensing of Environment 128, 150–161. doi:https://doi.org/10.1016/j.rse.2012.10.015.

Colbran, N., 2009. Will Jakarta be the next Atlantis? Excessive Groundwater Use resulting from a Failing Piped Water Network. Law, Environment

and Development Journal 5, 18. URL: http://www.lead-journal.org/content/09018.pdf.

Ekkelenkamp, H., 2019. Indonesië op de Kaart: De Rol van de Nederlandse Aanwezigheid in Indonesië bij de Ontwikkeling van de Geodesie in Nederland .

Fenoglio-Marc, L., Schöne, T., Illigner, J., Becker, M., Manurung, P., Khafid, 2012. Sea Level Change and Vertical Motion from Satellite Altimetry, Tide Gauges and GPS in the Indonesian Region. Marine Geodesy 35, 137–150. doi:https://doi.org/10.1080/01490419.2012.674063.

Ferretti, A., Prati, C., Rocca, F., 2002a. Nonlinear Subsidence Rate Estimation using Permanent Scatterers in Differential SAR Interferometry. IEEE Transactions on Geoscience and Remote Sensing 38, 2202–2212. doi:https://doi.org/10.1109/36.868878.

Ferretti, A., Prati, C., Rocca, F., 2002b. Permanent Scatterers in SAR Interferometry. IEEE Transactions on Geoscience and Remote Sensing 39, 8–20. doi:https://doi.org/10.1109/36.898661.

Firman, T., Surbakti, I.M., Idroes, I.C., Simarmata, H.A., 2011. Potential Climate-Change related Vulnerabilities in Jakarta: Challenges and current Status. Habitat International 35, 372–378. doi:https://doi.org/10.1016/j.habitatint.2010.11.011.

Gunawan, E., Widiyantoro, S., Hussain, E., Hanifa, N.R., Syafiudin, M.F., Wibowo, S.T., 2025. GNSS Constraints on the Jakarta Fault, Indonesia: Resolving Slip Rate and Seismic Hazard Potential. Earthquake Research Advances , 100424doi:https://doi.org/10.1016/j.eqrea.2025.100424.

Hakim, W.L., Achmad, A.R., Eom, J., Lee, C.W., 2020. Land Subsidence Measurement of Jakarta Coastal Area using Time Series Interferometry with Sentinel-1 SAR Data. Journal of Coastal Research 102, 75–81. doi:https://doi.org/10.2112/SI102-010.1.

Hanssen, R.F., 2001. Radar Interferometry: Data Interpretation and Error Analysis. Springer. doi:https://doi.org/10.1007/0-306-47633-9_4.

Hanssen, R.F., 2017. A radar retroreflector device and a method of preparing a radar retroreflector device. URL: https://patentimages.storage.googleapis.com/fe/ad/46/df362a63c8ed57/WO2018236215A1.pdf. patent WO 2018/236215 Al.

Harintaka, H., Suhadha, A.G., Syetiawan, A., Ardha, M., Rarasati, A., 2024. Current Land Subsidence in Jakarta: A multi-track SBAS InSAR Analysis during 2017–2022 using C-band SAR Data. Geocarto International 39, 2364726. doi:https://doi.org/10.1080/10106049.2024.2364726.

Herring, T.A., King, R.W., McClusky, S.C., et al., 2010. Introduction to GAMIT/GLOBK. Massachusetts Institute of Technology, Cambridge, Massachusetts 400, 401.

Hooper, A., 2008. A multi-temporal InSAR Method incorporating both Persistent Scatterer and Small Baseline Approaches. Geophysical Research Letters 35. doi:https://doi.org/10.1029/2008GL034654.

Hu, F., Wu, J., Chang, L., Hanssen, R.F., 2019. Incorporating temporary coherent scatterers in multi-temporal insar using adaptive temporal subsets. IEEE transactions on geoscience and remote sensing 57, 7658–7670.

Juliandri, F., Andreas, H., Pradipta, D., 2022. Efek Akurasi dan Geometrik Sistem Tinggi Digital Elevation Model (DEM) terhadap Pemodelan Banjir Rob di Jakarta. Bulletin of Geology 6, 934–948.

Kampes, B.M., 2006. Radar Interferometry: Persistent Scatterer Technique. Springer, Berlin.

Koudogbo, F.N., Duro, J., Arnaud, A., Bally, P., Abidin, H.Z., Andreas, H., 2012. Combined X- and L-Band PSI Analyses for Assessment of Land Subsidence in Jakarta, in: Remote Sensing for Agriculture, Ecosystems, and Hydrology XIV, pp. 46–58. doi:https://doi.org/10.1117/12.974821.

Kratzsch, H., 2012. Mining Subsidence Engineering. Springer Science & Business Media. doi:https://doi.org/10.1007/BF02509900.

Kreemer, C., Blewitt, G., Klein, E.C., 2014. A Geodetic Plate Motion and Global Strain Rate Model. Geochemistry, Geophysics, Geosystems 15, 3849–3889. doi:https://doi.org/10.1002/2014GC005407.

Lubis, S.W., Hagos, S., Hermawan, E., Respati, M.R., Ridho, A., Risyanto, Paski, J.A., Muhammad, F.R., Siswanto, Ratri, D.N., et al., 2022. Record-Breaking Precipitation in Indonesia's Capital of Jakarta in early January 2020 linked to the Northerly Surge, Equatorial Waves, and MJO. Geophysical Research Letters 49, e2022GL101513. doi:https://doi.org/10.1029/2022GL101513.

Mahapatra, P., van der Marel, H., van Leijen, F., Samiei-Esfahany, S., Klees, R., Hanssen, R., 2018. InSAR Datum Connection Using GNSS-Augmented Radar Transponders. Journal of Geodesy 92, 21–32. doi:https://doi.org/10.1007/s00190-017-1041-y.

Murdohardono, D., Sudarsono, U., 1998. Land Subsidence Monitoring System in Jakarta, in: Proceedings of Symposium on Japan-Indonesia IDNDR Project: Volcanology, Tectonics, Flood and Sediment Hazards, pp. 243–256.

Ng, A.H.M., Ge, L., Li, X., Abidin, H.Z., Andreas, H., Zhang, K., 2012. Mapping Land Subsidence in Jakarta, Indonesia using Persistent Scatterer Interferometry (PSI) Technique with ALOS PALSAR. International Journal of Applied Earth Observation and Geoinformation 18, 232–242. doi:https://doi.org/10.1016/j.jag.2012.01.018.

Nugraha, G.U., Bakti, H., Lubis, R.F., Nur, A.A., 2024. Jakarta Groundwater Modeling: A Review. Applied Water Science 14, 186.

Sagala, S., Lassa, J., Yasaditama, H., Hudalah, D., 2013. The Evolution of Risk and Vulnerability in Greater Jakarta: Contesting Government Policy. Institute for Resource Governance and Social Change, Kupang, Indonesia .

Schepers, J., 1926. De Nauwkeurigheidswaterpassing van Java, de Primaire Kringen 1a en ii, benevens het Stadsnet van Batavia en Weltevreden. Verhandelingen No. 1, Topografische Dienst in Nederlandsch-Indië .

Schuitenvoerder, H., 1926. De Nauwkeurigheidswaterpassing van Java. Jaarverslag van den Topografischen Dienst in Nederlandsch-Indië 1925.

Sidiq, T.P., Gumilar, I., Abidin, H.Z., Meilano, I., Purwarianti, A., Lestari, R., 2025. Spatial Distribution and Monitoring of Land Subsidence using

Sentinel-1 SAR Data in Java, Indonesia. Applied Sciences 15. doi:https://doi.org/10.3390/app15073732.

Su, G., Xiong, C., Zhan, W., 2026. ID-GInSAR: An Improved Methodology for Integrating GNSS to Enhance InSAR-Based Deformation Monitoring. Geophysical Journal International 244, ggaf430. doi:https://doi.org/10.1093/gji/ggaf430.

Susilo, S., Salman, R., Hermawan, W., Widyaningrum, R., Wibowo, S.T., Lumban-Gaol, Y.A., Meilano, I., Yun, S.H., 2023. GNSS Land Subsidence Observations along the Northern Coastline of Java, Indonesia. Scientific Data 10, 421. doi:https://doi.org/10.1038/s41597-023-02274-0.

Taftazani, R., Kazama, S., Takizawa, S., 2022. Spatial Analysis of Groundwater Abstraction and Land Subsidence for Planning the Piped Water Supply in Jakarta, Indonesia. Water 14, 3197. doi:https://doi.org/10.3390/w14203197.

Takagi, H., Esteban, M., Mikami, T., Fujii, D., 2016. Projection of Coastal Floods in 2050 Jakarta. Urban Climate 17, 135–145. doi:https://doi.org/10.1016/j.uclim.2016.05.003.

United Nations, 2025. World Urbanization Prospects 2025: Summary of Results. Technical Report UN DESA/POP/2025/TR/NO. 12. United Nations, , Department of Economic and Social Affairs, Population Division. New York.

Van Leijen, F.J., 2014. Persistent Scatterer Interferometry Based on Geodetic Estimation Theory. Ph.D. thesis. Netherlands Geodetic Commission (NCG). Amersfoort, The Netherlands.

Widodo, J., Herlambang, A., Sulaiman, A., Razi, P., Perissin, D., Kuze, H., Sumantyo, J.T.S., 2019. Land Subsidence Rate Analysis of Jakarta Metropolitan Region based on D-InSAR Processing of Sentinel Data C-band Frequency, in: Journal of Physics: Conference Series, p. 012004. doi:https://doi.org/10.1088/1742-6596/1185/1/012004.

Yong, C.Z., Denys, P.H., Pearson, C.F., 2017. Present-day kinematics of the Sundaland plate. Journal of Applied Geodesy 11, 169–178. doi:10.1515/jag-2016-0024.

Zebker, H.A., Villasenor, J., 1992. Decorrelation in Interferometric Radar Echoes. IEEE Transactions on Geoscience and Remote Sensing 30, 950–959. doi:https://doi.org/10.1109/36.175330.

Zhang, J., Duan, W., Fu, X., Yun, Y., Lv, X., 2025. The stepwise multi-temporal Interferometric Synthetic Aperture Radar with partially Coherent Scatterers for long-time Series Deformation Monitoring. Remote Sensing 17, 1374. doi:https://doi.org/10.3390/rs17081374.